ACS APPLIED MATERIALS & INTERFACES

www.acsami.org

Research Article

Molecular Simulation of CO_2/CH_4 Transport and Separation in Polystyrene-*block*-poly(ethylene oxide)/Ionic Liquid (IL) Membranes: Insights into Nanoconfined IL Effects

Azam Salmankhani, Alexander M. Lopez, Paul Scovazzo, Adam E. Smith, and Sasan Nouranian*

Cite This: *ACS Appl. Mater. Interfaces* 2025, 17, 11348−11361

Read Online

ACCESS | Metrics & More | Article Recommendations

ABSTRACT: The phenomenon of ionic liquid (IL) nanoconfinement within a copolymer/IL membrane reportedly enhances membrane selectivity, solubility, and transport in gas separations. Also, the copolymer/IL membrane morphology has been found to affect IL stability at high transmembrane pressures. In this work, a combined mesoscopic dynamics simulation and hybrid grand canonical Monte Carlo/molecular dynamics (GCMC-MD) simulations were carried out to investigate the morphologies, as well as CO_2/CH_4 gas diffusivities, solubilities, and selectivities of polystyrene-*b*-poly(ethylene oxide) (PS-*b*-PEO)/1-Ethyl-3-methylimidazolium thiocyanate ([EMIM][SCN]) and PS-*b*-PEO/1-Ethyl-3-methylimidazolium bis(trifluoromethylsulfonyl)imide ([EMIM]-[Tf_2N]) membranes. The latter simulations focused on nanoconfined ILs in the copolymer/IL phase boundaries at 2.5 and 5 nm confinement lengths. The investigated systems were four nanoconfined ILs, i.e., PS/[EMIM][SCN]/PEO (the IL forming a separate microphase, denoted IL-Micro), PS/[EMIM][Tf_2N]/PEO, PS/[EMIM][SCN]-PEO/PS (the IL distributed in the PEO phase, denoted IL-PEO), and PS/[EMIM][Tf_2N]-PEO/PS, and five control systems, i.e., PS/PEO/PS, bulk PS, bulk PEO, bulk [EMIM][SCN], and bulk [EMIM][Tf_2N]. Based on the mesoscopic dynamics simulation results, the dominant membrane morphologies at IL loadings of <50 vol % were lamellar or cylindrical (favorable for both IL stability at high transmembrane pressures if the bedding planes are horizontal, i.e. at 90° to the nominal direction of the transmembrane pressure gradient) with the IL-PEO or IL-Micro phases. Also, there was an overall 50% match between the observed PS-*b*-PEO/[EMIM][SCN] and PS-*b*-PEO/[EMIM][Tf_2N] membrane morphologies. Based on the MD simulation results, both CO_2 and CH_4 diffusivities were the smallest in the bulk PS (control) and highest in the PS/[EMIM][Tf_2N]/PEO system (IL-Micro between the PS and PEO phases) at both confinement lengths. The CO_2 diffusivities were, on average, larger when the confinement length increased to 5 nm. The GCMC-MD results indicated that the CO_2 solubility in the IL-Micro phases was higher than in the corresponding bulk ILs at both confinement lengths, with the PS/[EMIM][Tf_2N]/PEO system exhibiting the highest CO_2 solubility, followed by the PS/[EMIM][SCN]/PEO system. Additionally, the permselectivities of the nanoconfined IL systems were, on average, 40−50% larger than those of the bulk systems, with the highest permselectivity observed for PS/[EMIM][Tf_2N]/PEO at the confinement length of 5 nm. Overall, the IL nanoconfinement between the PS and PEO phases (IL-Micro) leads to significant improvements in the CO_2/CH_4 permselectivities, suggesting that strategies to create nanoconfined IL morphologies in the copolymer/IL membranes are very promising for optimizing the membrane gas separation performance.

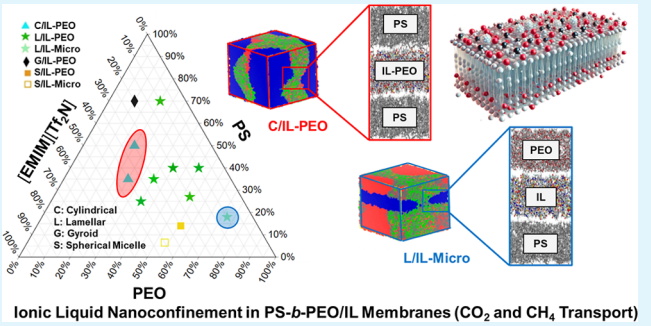

KEYWORDS: *copolymer/ionic liquid membrane, morphology, nanoconfinement, mesoscopic dynamics simulation, grand canonical Monte Carlo-molecular dynamics simulation, gas transport, gas separation*

INTRODUCTION

Block copolymer membranes have garnered significant attention in gas separation applications due to their tunable morphologies, as well as favorable thermal, chemical, and mechanical stability.[1] These copolymers consist of two chemically distinct constituent blocks that are covalently bound, creating a morphology with favorable pathways for separating gases with different molecular sizes and polarities.[2] When integrated with ionic liquids (ILs), the block copolymer membranes offer enhanced gas separation

Received: November 30, 2024
Revised: January 23, 2025
Accepted: January 29, 2025
Published: February 6, 2025

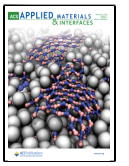

https://doi.org/10.1021/acsami.4c21064
ACS Appl. Mater. Interfaces 2025, 17, 11348−11361

performance due to the synergism arising from the copolymer morphology and selective gas absorption and transport properties of the IL.[3] In general, incorporating ILs into block copolymers improves the gas selectivity of the membrane and also contributes to its thermal and chemical stability. The resulting hybrid membrane exhibits superior gas separation performance.[4]

Diblock copolymer membranes have a variety of self-assembled morphologies, such as body-centered cubic (BCC) spheres, hexagonally packed cylinders (HPC), gyroids (G), or lamellae (L), which significantly influence the gas separation characteristics of the membranes.[5] The IL incorporation into block copolymers leads to more complicated morphologies. For example, the self-assembled morphologies of a polystyrene-*b*-poly(ethylene oxide) (PS-*b*-PEO)/1-Ethyl-3-methylimidazolium thiocyanate ([EMIM][SCN]) system include cylindrical (C), L, BCC, G, or spherical micelles (S) morphologies, where the IL is either distributed in the PEO phase or forms a separate microphase (Figure 1).[6] Adzima et al.[7] reported the formation of

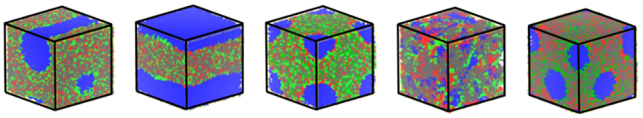

Figure 1. Representative self-assembled morphologies of PS-*b*-PEO/[EMIM][SCN] at 298 K and different PS/PEO block size ratios and IL loadings. The morphologies are identified as cylindrical (C), lamellar (L), body-centered cubic (BCC), gyroid (G), and spherical micelle (S), where the IL is distributed in the PEO phase (IL-PEO) (adapted from ref 13; copyright 2023 American Chemical Society). Color codes: blue: PS, red: PEO, gray: [EMIM] cation, and green: [SCN] anion.

a phase-separated morphology in poly(methyl methacrylate)-*b*-P(P888 allyl Tf_2N) membrane with a CO_2 permeability of 71 barrer and CO_2/N_2 selectivity of 20. In contrast, the nonphase-separated membrane exhibited a significantly lower permeability of 24 barrer. The choice of IL and the stabilization of the IL phase within the copolymer also play a prominent role in achieving desired gas permeability and selectivity. In particular, imidazolium-based ILs are frequently selected for gas transport applications due to their high thermal stability and favorable ionic conductivity, contributing to enhanced gas solubility and diffusivity. For example, [EMIM][SCN] offers high CO_2/N_2 selectivity,[8] making it ideal for CO_2 capture, while 1-Ethyl-3-methylimidazolium bis(trifluoromethylsulfonyl)imide ([EMIM][Tf_2N]) provides superior CO_2 solubility.[9]

To further enhance the gas separation performance of block copolymer/IL membranes, nanoconfinement of one phase, typically the IL or IL-containing phase, by the other phases has been explored.[10] In general, the IL nanoconfinement significantly alters the overall gas-membrane molecular interactions, resulting in improved gas solubility, diffusivity, and selectivity.[11] The IL distribution within the polymer phases and evolution of IL nanoconfinement within a copolymer/IL membrane is thermodynamically driven and depends on the chemical structure of the copolymer blocks, IL loading, and temperature.[12] The equilibrium self-assembled membrane morphology has often been observed to provide favorable pathways for gas diffusion and to create localized pressure zones within the nanopores,[13] thereby improving the overall membrane separation performance. Moreover, IL nanoconfinement often leads to improved stability of the IL phase within the copolymer through the restriction of IL mobility and increasing the polymer-IL interfacial interactions.[14] This stabilization prevents IL displacement, a significant issue for membranes at elevated pressures, and ensures consistent gas separation performance.[15]

Recent research has provided valuable insights into the effects of IL nanoconfinement on gas separation performance in copolymer/IL membranes. For example, studies have shown that IL nanoconfinement within a polymeric or porous framework can significantly enhance CO_2 permeability and selectivity over other gases, such as CH_4 and N_2.[16,17] Wang et al.[18] reported that the nanoconfinement of 1-Ethyl-3-methylimidazolium acetate ([EMIM][Ac]) in TCOH@Pebax-1657 2D mixed-matrix membranes could improve CO_2 permeance and CO_2/N_2, as well as CO_2/CH_4 selectivity, up to an IL loading of 3.5 wt %. In another study, Rahmani et al.[19] reported favorable CO_2/CH_4 separation performance in membranes where [EMIM][SCN] was nanoconfined by polyvinylidene fluoride (PVDF). Their results demonstrated that PVDF-confined IL could improve CO_2/CH_4 permselectivity by 72% compared to the bulk IL. In another study, Chen et al.[20] demonstrated excellent CO_2 separation performance in molybdenum disulfide (MoS_2)-confined 1-Butyl-3-methylimidazolium tetrafluoroborate ([BMIM][BF_4]) laminated membranes. They reported a CO_2 permeance of ∼48 GPU and improved selectivity for CO_2/N_2 (∼131), CO_2/H_2 (∼15), and CO_2/CH_4 (∼44), compared to the bulk IL. In yet another study, Tian et al.[21] investigated gas separation in membranes where 1-Butyl-3-methylimidazolium bis(trifluoromethylsulfonyl)imide ([BMIM][TfSI]) was confined within a charged porous polymer nanocomposite. They reported that the IL nanoconfinement improved CO_2 solubility and CO_2/CH_4 selectivity, while diffusivity was lower in the polymer-confined IL than in the bulk polymer. Tan et al.[22] reported that a mesoporous phenolic resin-confined [EMIM][BF_4] membrane (pore size: ∼7 nm) supported on alumina (Al_2O_3) shows higher CO_2 permeance than a macroporous poly(ether sulfone) (PES)-confined [EMIM][BF_4] membrane (pore size: ∼450 nm) on the same support at different transmembrane pressures. They also reported a CO_2/N_2 selectivity of 40 and higher stability for the mesoporous phenolic resin/IL membrane than those of the macroporous PES/IL membrane. Min et al.[23] investigated CO_2/N_2 separation in poly(ethylene glycol) methyl ether (mPEG)-*b*-polyacrylonitrile (PAN)/1-Ethyl-3-methylimidazolium dicyanamide ([EMIM][DCA]) membranes. Based on their results, efficient IL nanoconfinement within a 3D bicontinuous nanostructured morphology resulted in a CO_2 permeability of ∼456 barrer. Moreover, a maximum CO_2/N_2 selectivity of ∼61 was obtained. In a similar study, Grünauer et al.[24] studied CO_2/N_2 separation in PS-*b*-poly(4-vinylpyridine) (P4VP)/IL membranes. They reported the highest CO_2/N_2 selectivity of 60, which was obtained for [EMIM][DCA]-confined membranes, followed by selectivities of 20 and 19 in [EMIM][Tf_2N]- and [BMIM][Ac]-confined membranes, respectively.

The above literature survey highlights the significance of membrane morphology, composition, and IL nanoconfinement in copolymer/IL membranes to their gas separation performance. Therefore, to optimize membrane fabrication to meet the stringent demands of industrial gas separations, a thorough understanding of the interplay between the copolymer and IL phases in the membrane morphology development, as well as the effects of IL nanoconfinement within the polymer phases, on its stabilization and alteration of gas solubility, selectivity, and transport properties are crucial. For this purpose, a combined

https://doi.org/10.1021/acsami.4c21064
ACS Appl. Mater. Interfaces 2025, 17, 11348−11361

mesoscopic dynamics/molecular dynamics (MD) simulation approach was used herein to investigate the morphologies and CO_2/CH_4 separation performances of two diblock copolymer/IL systems, i.e., PS-*b*-PEO/[EMIM][SCN] and PS-*b*-PEO/[EMIM][Tf_2N]. The two selected ILs, i.e., [EMIM][Tf_2N] and [EMIM][SCN], are known to have Kamlet−Taft solvent parameters[25] that are low (β = 0.42) and high (β = 0.71), respectively, making them suitable for studying IL selectivity and copolymer/IL interactions. Although the β-parameter difference between the ILs seems small, studies show that gas selectivity increases exponentially with β.[26] The use of the common [EMIM] cation is motivated by its consistently high selective performance[27] and the minimal impact of the cation size on the β parameter.[28]

Building upon a previous work[6] that explored the self-assembled morphologies of PS-*b*-PEO/[EMIM][SCN] membranes using mesoscopic dynamics simulation, herein, the morphology investigation is first extended to the PS-*b*-PEO/[EMIM][Tf_2N]. The main objective was to compare the resulting morphologies of PS-*b*-PEO/[EMIM][Tf_2N] to those of PS-*b*-PEO/[EMIM][SCN] in a region of their ternary phase diagrams that are favorable for gas separations. Next, by conducting all-atom MD simulations on the selected morphologies from these two IL systems, the CO_2/CH_4 mixed-gas diffusivity, solubility, and selectivity were examined to gain insights into favorable nanoconfined IL morphologies for CO_2/CH_4 separation. Although MD simulation has been previously applied to polymer/IL membranes, this work uniquely examines the effects of IL nanoconfinement within a copolymer, filling a gap in the literature that could lead to new strategies for designing efficient gas separation membranes.

COMPUTATIONAL METHODS

Mesoscopic Dynamics Simulation Details. Following the methodology developed by Salmankhani et al.,[6] the dynamic mean-field density functional theory method[29,30] was used to perform a series of mesoscopic dynamics simulations of PS-*b*-PEO/[EMIM][Tf_2N] for different IL loadings and copolymer block size ratios. Briefly, the fundamental building block in the dynamic mean-field density functional theory method is a coarse-grained (CG) Gaussian chain of a polymer composed of a series of interconnected beads with springs (the bead−spring model). For an AB block copolymer at the mesoscale, the Gaussian chain contains $N = N_A + N_B$ beads, where the bead-chain topology obeys the following equation

$$N_{meso} = \frac{M_p}{M_m C_\infty} \quad (1)$$

where, M_p is the molecular weight of the polymer, M_m is the molecular weight of the monomer, and C_∞ is the characteristic ratio of the polymer. The C_∞ values for PS and PEO are 9.9 and 5, respectively. These values were obtained from the Synthia module of Materials Studio v2022 software. The CG models of PS-*b*-PEO block copolymer, [EMIM] cation, and [Tf_2N] anion are shown in Figure 2, where the bead selections were such that similar bead masses and volumes were achieved. This approach maintains the CG topologies proposed by the well-known CG models, i.e., Martini.[31] Table 1 provides the real and CG chain topologies of the corresponding PS-*b*-PEO blends.

In a real PS-*b*-PEO/[EMIM][Tf_2N] membrane, the IL needs to be stabilized within the copolymer phase to withstand high transmembrane pressures. This is to maximize the capillary forces that resist IL displacement by the transmembrane pressures, thereby rendering the membrane stable for gas separation.[32,33] For this purpose, the membrane morphology needs to be fine-tuned. It has been reported that cylindrical or lamellar morphologies, with the IL nanoconfined within the ionophilic cylindrical and/or lamellar domains[34] may be

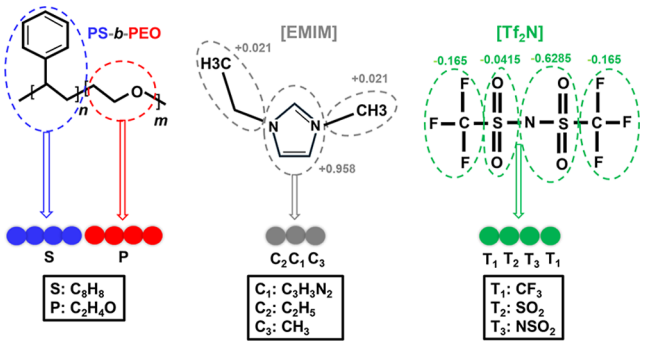

Figure 2. Molecular structures and corresponding coarse-grained models for the PS-*b*-PEO copolymers and [EMIM][Tf_2N]. The blue and red beads represent the hydrophobic PS and hydrophilic PEO chains of the diblock copolymer, respectively. Gray and green beads represent the coarse-grained [EMIM] cations and [Tf_2N] anions, respectively. The partial charges assigned to beads C_1, C_2, and C_3 add up to a total charge of +1 for the [EMIM] cation, and the partial charges assigned to beads T_1, T_2, and T_3 add up to a total of −1 for the [Tf_2N] anion.

Table 1. Real and Coarse-Grained Chain Topologies of the PS-*b*-PEO Block Copolymers

real-chain topology[a]	coarse-grained chain topology[b]	coarse-grained block size ratio
PS200−PEO100	PS20−PEO20	1:1
PS100−PEO100	PS10−PEO20	1:2
PS200−PEO50	PS20−PEO10	2:1
PS100−PEO200	PS10−PEO40	1:4
PS200−PEO125	PS20−PEO25	4:5
PS250−PEO100	PS25−PEO20	5:4
PS50−PEO200	PS5−PEO40	1:8
PS140−PEO10	PS14−PEO2	7:1
PS140−PEO20	PS14−PEO4	7:2

[a]Real chain block sizes are indicated by the number of polymer repeating units (monomers). [b]Coarse-grained block size ratios, indicated by the number of attached beads.

favorable for minimal IL displacement. The ternary phase diagram of PS-*b*-PEO/[EMIM][SCN][6] revealed that the morphologies of interest for CO_2/CH_4 separation (lamellar and cylindrical) are likely to form at IL loadings below 50 vol % for a variety of PS/PEO block size ratios, as shown in Figure 3a. Therefore, 12 diblock copolymer/IL configurations were targeted in the same region of the phase diagram for exploring the PS-*b*-PEO/[EMIM][Tf_2N] morphologies (Figure 3b).

To run a mesoscopic dynamics simulation, the extended Flory−Huggins interaction parameters, X_{ij}, were determined. For this purpose, the beads were geometrically optimized using the condensed-phase optimized molecular potentials for atomistic simulation studies (COMPASS III) force field,[35] excluding electrostatics, after which the interaction parameters between the beads were calculated based on the solution model developed by Fan et al.[36] The COMPASS force field with its three iterations (I, II, and III) is widely used to accurately model systems containing carbon, hydrogen, oxygen, nitrogen, sulfur, and fluorine (C/H/O/N/S/F) atoms, particularly in condensed phases like liquids. The X_{ij} interaction parameters were then converted to the repulsion parameters (A_{ij}) of the beads using the following equation

$$A_{ij} = \nu^{-1}\varepsilon_{ij} = \chi_{ij}RT \text{ (kJ/mol)} \quad (2)$$

where ν is the statistical volume of a bead. The calculated values for X_{ij} and A_{ij} are listed in Table 2.

After explicitly applying partial charges to the charged beads (Figure 2) and setting the simulation parameters, all mixtures were equilibrated

https://doi.org/10.1021/acsami.4c21064
ACS Appl. Mater. Interfaces 2025, 17, 11348−11361

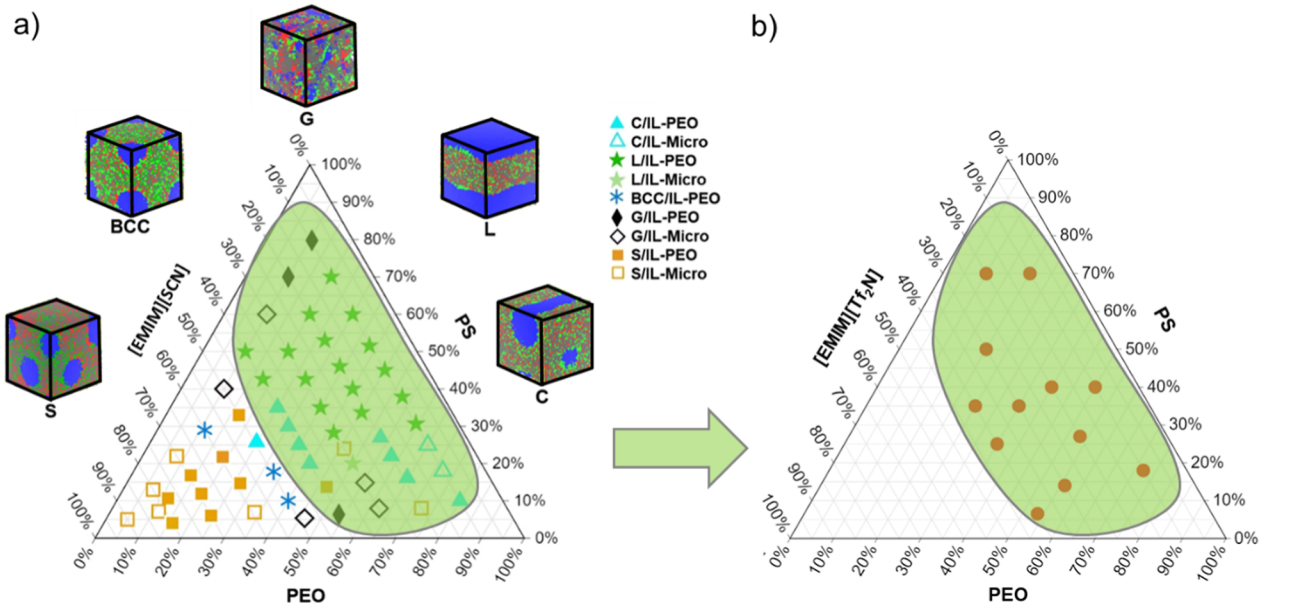

Figure 3. (a) Ternary phase diagram of PS-*b*-PEO/[EMIM][SCN] at 298 K (reproduced from ref 13; Copyright 2023 American Chemical Society). The IL loadings are on a volume basis. Copolymer morphology is designated as C: cylindrical, L: lamellar, BCC: body-centered cubic, G: gyroid, and S: spherical micelle. The IL morphology is designated as IL-PEO: IL distributed in the PEO phase and IL-Micro: IL forming a separate microphase. The morphologies of interest for CO_2/CH_4 separation are enclosed in the green-highlighted region. (b) The 12 PS-*b*-PEO/[EMIM][Tf_2N] membrane configurations within the green-highlighted region selected for mesoscopic dynamics simulations. Color codes: blue: PS, red: PEO, gray: [EMIM] cation, and green: [SCN] anion.

Table 2. Flory–Huggins (χ_{ij}) and Repulsion Parameters (A_{ij}) for the Coarse-Grained PS-*b*-PEO/[EMIM][Tf_2N] at 298 K

bead type[a]	*S*		*P*		C_1		C_2		C_3		T_1		T_2	
	χ_{ij}	A_{ij}[b]	χ_{ij}	A_{ij}	χ_{ij}	A_{ij}	χ_{ij}	A_{ij}	χ_{ij}	A_{ij}	χ_{ij}	A_{ij}	χ_{ij}	A_{ij}
S	0.00	**0.00**												
P	1.85	4.58	0.00	**0.00**										
C_1	1.53	3.79	0.19	**0.46**	0.00	**0.00**								
C_2	2.17	5.37	0.06	**0.14**	0.46	**1.13**	0.00	**0.00**						
C_3	3.32	8.22	0.41	**1.01**	1.01	**2.5**	0.14	**0.34**	0.00	**0.00**				
T_1	1.04	2.57	−0.08	**−0.19**	0.09	**0.22**	0.07	**0.17**	0.5	**1.23**	0.00	**0.00**		
T_2	1.91	4.73	−0.11	**−0.27**	0.07	**0.17**	0.04	**0.09**	0.52	**1.28**	−0.02	**−0.04**	0.00	**0.00**
T_3	2.17	5.37	0.05	**0.12**	0.45	**1.11**	−0.006	**−0.01**	0.16	**0.39**	0.06	**0.14**	**0.07**	**0.17**

[a]Bead types: S: PS; P: PEO; C_1: imidazolium ring of [EMIM]; C_2 and C_3: side chains of [EMIM]; T_1, T_2 and T_3: [Tf_2N]. [b]Unit: kJ/mol.

for at least 100,000 steps at 298 K with a time step of 50 ns and a total simulation time of 5 ms.

Molecular Dynamics Simulation Details. *Models of the Nanoconfined IL Systems.* Herein, four models of nanoconfined ILs within the PS-*b*-PEO copolymer were constructed in BIOVIA Materials Studio v2022 at two confinement lengths of 2.5 (cell dimension: 10 × 10 × 7.5 nm^3) and 5 nm (cell dimension: 10 × 10 × 10 nm^3) (Figure 4). The 3D-periodic systems comprise (1) the IL distributed in the PEO phase and nanoconfined between the PS domains, designated as PS/[EMIM][SCN]-PEO/PS (Figure 4a) and PS/[EMIM][Tf_2N]-PEO/PS (Figure 4b), and (2) IL forming a microphase, nanoconfined between the PS and PEO domains, designated as PS/[EMIM][SCN]/PEO (Figure 4c) and PS/[EMIM][Tf_2N]/PEO (Figure 4d). In addition, a model of PS/PEO/PS (no IL) (Figure 4e) and four models of bulk systems, i.e., bulk PS, Bulk PEO, bulk [EMIM][SCN], and bulk [EMIM][Tf_2N] (Figure 4f) with the cell dimensions of 10 × 10 × 2.5 nm^3 and 10 × 10 × 5 nm^3 were constructed as controls. The two sizes for the bulk systems were selected to match the confinement lengths of 2.5 and 5 nm for the nanoconfined IL systems. The PS and PEO blocks in the copolymers were created with ten monomer units. Also, the number of copolymer chains and ion pairs varied between the systems, depending on the relevant structure and confinement length, while the IL loading was kept constant at 40 vol %. The initial target density of the systems was 1 g/cm^3. All structures were geometry-optimized at 298 K using the conjugate gradient method.[37] The OPLS-AA force field[38,39] was used for the ILs and PEO, and the consistent valence force field (CVFF) was used for PS. Both force fields have been proven to be accurate in predicting the properties of ILs and polymers.[40,41]

Also, the partial atomic charges and force field parameters of CO_2 were adopted from the EPM2 model, which has been shown to provide more accurate results compared to other models such as TraPPE and MSM.[42] For CH_4, the parameters were adopted from the OPLS-AA[43] model to ensure consistency with the force fields used for PEO and IL. For the ILs, the partial charges were derived from the work of Sambasivarao and Acevedo,[39] and applied to the cations and anions before geometry optimization. For PEO, the OPLS-AA partial charges were first generated in the LigParGen[44] Web server using the CM1A-LBCC charge model with a scaling factor of 1.14 for neutral molecules and then applied to the atoms before geometry optimization. For PS, the partial charges were assigned by the CVFF during geometry optimization.[45,46] Next, the structures and force field data were exported to the open-source large-scale atomic/molecular massively parallel simulator (LAMMPS) software. The force field atom types in the different structures (polymers, ILs, CO_2, and CH_4) and the corresponding force field parameters and partial atomic charges are provided in Figure 5 and Table 3, respectively.

https://doi.org/10.1021/acsami.4c21064
ACS Appl. Mater. Interfaces 2025, 17, 11348−11361

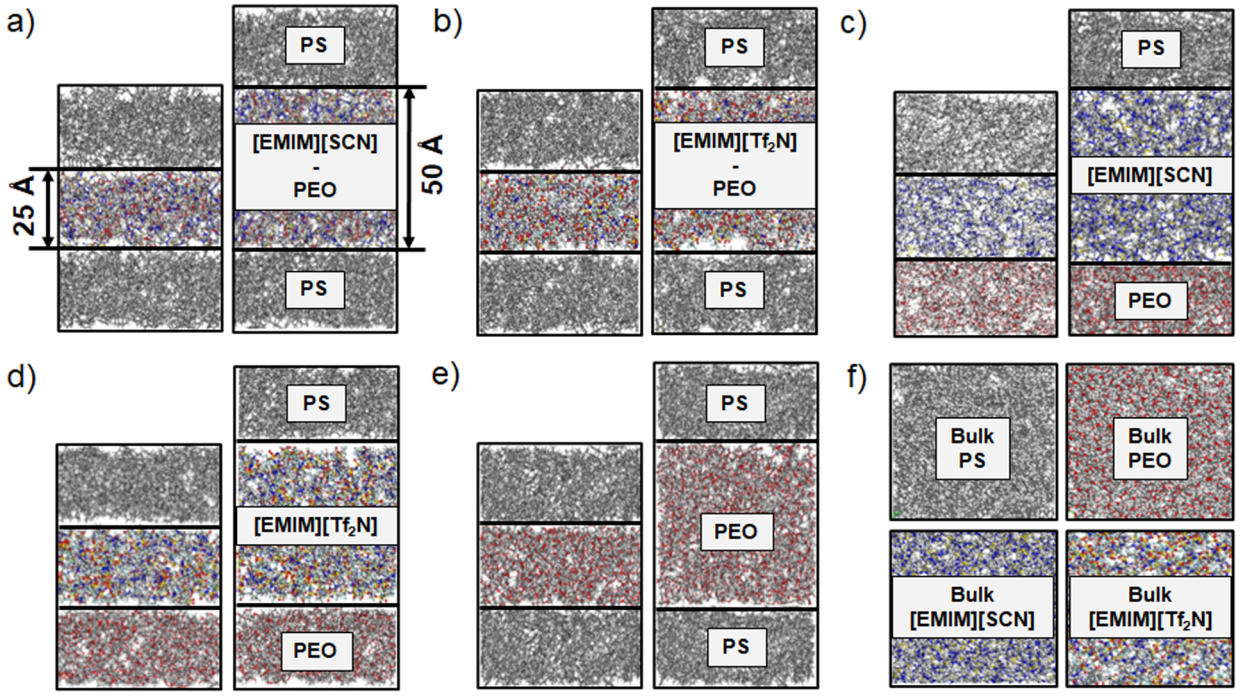

Figure 4. Snapshots of the initial structures of the nanoconfined ILs within PS-*b*-PEO and control bulk systems: (a) PS/[EMIM][SCN]-PEO/PS, (b) PS/[EMIM][Tf_2N]-PEO/PS, (c) PS/[EMIM][SCN]/PEO, (d) PS/[EMIM][Tf_2N]/PEO, (e) PS/PEO/PS (control), and (f) bulk PS, bulk PEO, Bulk [EMIM][SCN], and bulk [EMIM][Tf_2N] (controls). The nanoconfined IL systems were constructed at two confinement lengths of 2.5 (cell dimension: $10 \times 10 \times 7.5$ nm^3) and 5 nm (cell dimension: $10 \times 10 \times 10$ nm^3). The the cell dimensions of the bulk systems were $10 \times 10 \times 2.5$ nm^3 and $10 \times 10 \times 5$ nm^3, corresponding to the two confinements lengths in the nanoconfined IL systems, respectively.

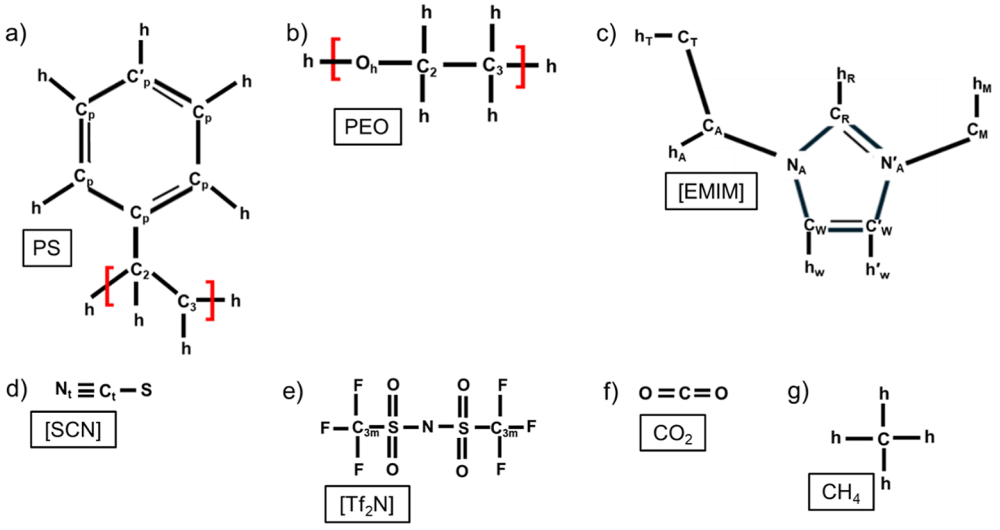

Figure 5. Force field atom types assigned to the polymers, ILs, and gas molecules: (a) PS: CVFF, (b) PEO: OPLS-AA, (c) [EMIM] cation: OPLS-AA, (d) [SCN] anion: OPLS-AA, (e) [Tf_2N] anion: OPLS-AA, (f) CO_2: EPM2, and (g) CH_4: OPLS-AA.

Thermal Equilibration of the Systems. All systems were simulated at 298 K and 1 atm for 5 ns with a time step of 1 fs using the isothermal–isobaric (*NPT*) ensemble to reach equilibrium density. The system temperature and pressure were controlled using the Nosé–Hoover thermostat[47] and barostat, respectively. The particle–particle–particle-mesh (PPPM) method[48] was used for long-range Coulombic interactions with a cutoff distance of 12 Å. The 12–6 Lennard–Jones (LJ) potential was used to calculate the nonbonded interactions[49] between two atoms

$$U(r) = 4\varepsilon\left[\left(\frac{\sigma_{ij}}{r_{ij}}\right)^{12} - \left(\frac{\sigma_{ij}}{r_{ij}}\right)^{6}\right], \quad r < r_c \tag{3}$$

where σ_{ij} is the LJ radius, ε is the potential energy, r_{ij} is the distance between atoms i and j, and r_c is the cutoff radius. In addition, the Lorentz–Berthelot mixing rule[50] was applied to calculate the LJ parameters between two nonbonded atoms i and j, by the following equations

$$\sigma_{ij} = \frac{\sigma_i + \sigma_j}{2} \tag{4}$$

https://doi.org/10.1021/acsami.4c21064
ACS Appl. Mater. Interfaces 2025, 17, 11348–11361

Table 3. Force Field Parameters and Partial Atomic Charges Assigned to the Polymers, ILs, and Gas Molecules

structure	forcefield atom type	partial charge (e)	ε_{ij} (kJ/mol)	σ_{ij} (Å)
PS	C_p	−0.1000	0.140	3.610
	C_p'	0.0000	0.140	3.610
	C_2	−0.2000	0.038	3.870
	C_3	−0.3000	0.038	3.870
	h	0.1000	0.038	2.440
PEO	C_2	0.1400	0.066	3.500
	C_3	0.1400	0.066	3.500
	O_h	−0.4000	0.170	3.120
	h	0.0300	0.030	2.500
[EMIM]	C_R	−0.0335	0.070	3.550
	C_W	−0.2154	0.070	3.550
	C_W'	−0.2336	0.070	3.550
	C_M	−0.3524	0.066	3.500
	C_A	0.0462	0.066	3.500
	C_T	−0.1417	0.066	3.500
	N_A	0.211	0.170	3.250
	N_A'	0.0998	0.170	3.250
	h_R	0.2109	0.030	2.420
	h_w	0.2604	0.030	2.420
	h_w'	0.2641	0.030	2.420
	h_A	0.0778	0.030	2.500
	h_T	0.0708	0.030	2.500
	h_M	0.1718	0.030	2.500
[SCN]	S	−0.6811	0.250	3.550
	C_t	0.3263	0.066	3.300
	N_t	−0.6452	0.170	3.250
[Tf_2N]	S	1.0200	0.250	3.550
	O	−0.5300	0.210	2.960
	N	−0.6600	0.170	3.250
	F	−0.1600	0.053	2.950
	C_{3m}	0.3500	0.066	3.500
CO_2	C	0.6512	0.055	2.757
	O	−0.3256	0.150	3.033
CH_4	C	−0.2400	0.066	3.500
	h	0.0600	0.030	2.500

$$\varepsilon_{ij} = \sqrt{\varepsilon_{ii} \times \varepsilon_{jj}} \tag{5}$$

This rule combines Lennard−Jones parameters using an arithmetic mean for size (σ) and a geometric mean for energy (ε), offering a balance of computational simplicity and accuracy, and is widely validated and extensively employed in heterogeneous systems, where electrostatic and dispersion forces dominate, e.g. gas-IL mixtures.[51] The average equilibrium densities of the bulk PS (1.12 g/cm^3), PEO (1.08 g/cm^3), [EMIM][SCN] (1.12 g/cm^3), and [EMIM][Tf_2N] (1.58 g/cm^3), obtained by averaging the system densities during the last 2 ns of thermal equilibration (Figure 6) were found to be in good agreement with the corresponding experimental densities of PS (~1.12 g/cm^3),[52] PEO (~1.09 g/cm^3),[53] [EMIM][SCN] (~1.12 g/cm^3),[52,54] and [EMIM][Tf_2N] (~1.52 g/cm^3).[54]

Simulation of the Gas Transport Properties. To calculate the CO_2 and CH_4 mixed-gas diffusivities, all systems were rebuilt with the equilibrium densities obtained at the end of the NPT simulations, after which 50 CO_2 and CH_4 molecules were directly inserted into the nanoconfined regions in the layered systems (Figure 4a−e) in an equimolar ratio and to the entire simulation box in the bulk systems (Figure 4f). Next, the systems were simulated at 298 K for 5 ns using the canonical (*NVT*) ensemble with a time step of 1 fs. Following the completion of the *NVT* simulations, the mean-square displacement (MSD) data for CO_2 and CH_4 were calculated during a dynamic production run for 2 ns at the same time step, temperature, and pressure

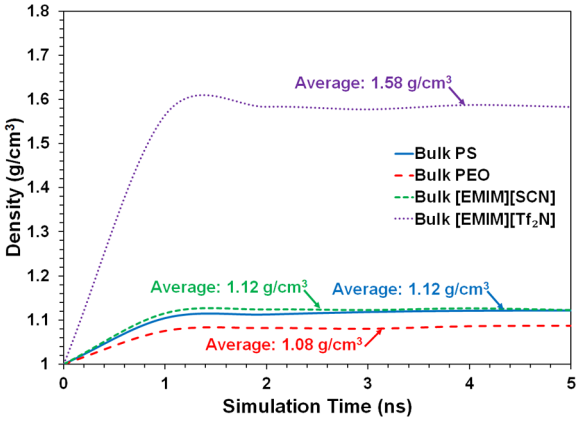

Figure 6. Density profiles of the bulk PS, PEO, [EMIM][SCN], and [EMIM][Tf_2N] during thermal equilibration of the systems for 5 ns.

from the time-series of positions of all atoms using the following equation (system trajectories collected every 1000 fs)

$$\text{MSD} \equiv \langle |r_i(t) - r_i(0)|^2 \rangle \tag{6}$$

where $r_i(t)$ is the position of the ith molecule at time t and $r_i(0)$ is the reference position of the ith molecule. Diffusivities (D) were then calculated by linear regression to the linear part of the MSD plot based on Einstein's relation[55]

$$D = \frac{1}{6N} \lim_{t\to\infty} \sum_{i=1}^{N} \langle |r_i(t) - r_i(0)|^2 \rangle \tag{7}$$

where N is the number of gas molecules to be averaged over. Next, the CO_2/CH_4 diffusivity selectivities were calculated by dividing the CO_2 diffusivity with that of CH_4 from the following equation

$$S^D_{CO_2/CH_4} = \frac{D_{CO_2}}{D_{CH_4}} \tag{8}$$

The production runs were replicated three times, and the resulting MSD data were averaged.

Simulations to Calculate Gas Solubilities and Selectivities. A series of hybrid grand canonical Monte Carlo (GCMC)-MD simulations were performed for the different systems to determine the gas solubilities and selectivities. For this purpose, the systems were first equilibrated using *NVT* simulations for 5 ns, after which GCMC-MD production runs were performed for 1 ns at 298 K and 1 atm to keep the gas reservoir in thermodynamic equilibrium with the nanoconfined IL systems. Using this method, the chemical potential of the gas phase is automatically calculated through the Metropolis algorithm,[56] which obeys the ideal gas equation of state. In this work, the GCMC exchange strokes were applied every 100 steps for 500 exchange MC moves. During the GCMC procedure, a random exchange of CO_2 and CH_4 gas molecules occurs between an implicit imaginary gas reservoir and the mixture, which can be either insertion or deletion with an equal probability. The exchange region was limited to the nanoconfined regions of the structures. The trajectories were collected every 500 fs to calculate the CO_2 and CH_4 mole-fraction-scaled solubility from the following equations

$$S_{CO_2} = \frac{x_{CO_2}}{(x_{CO_2} + x_{\text{other components in the exchange region}})} S_{CH_4} = \frac{x_{CH_4}}{(x_{CH_4} + x_{\text{other components in the exchange region}})} \tag{9}$$

where x_{CO_2} and x_{CH_4} are the mole fractions of the gas molecules. The CO_2/CH_4 solubility selectivities were then obtained from the following equation

https://doi.org/10.1021/acsami.4c21064
ACS Appl. Mater. Interfaces 2025, 17, 11348−11361

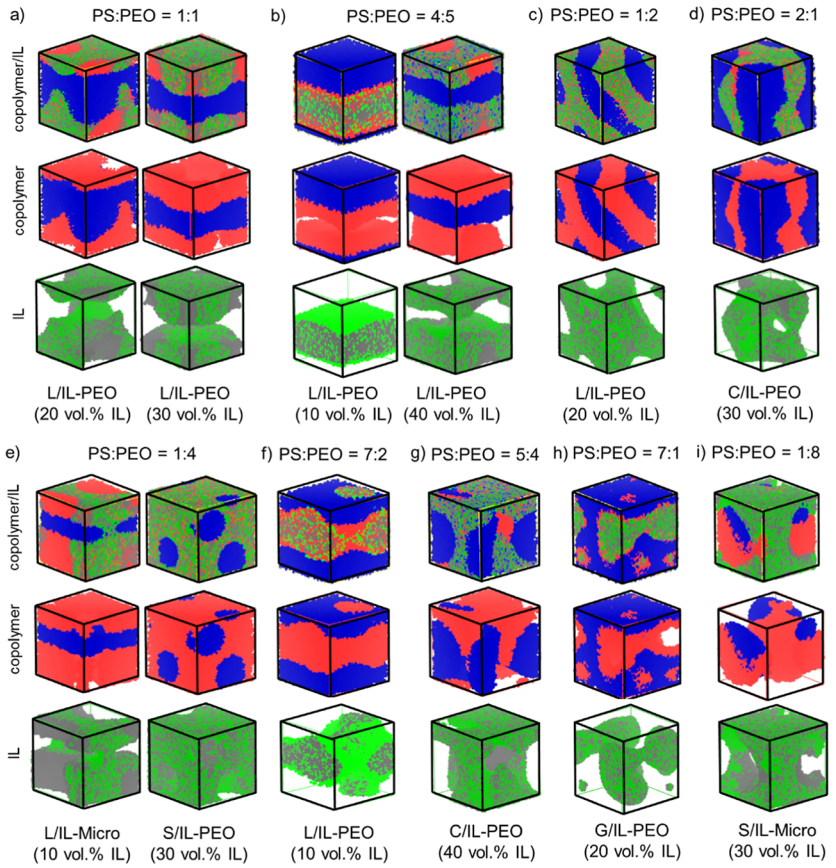

Figure 7. Representative lamellar (L), cylindrical (C), gyroid (G), and spherical micelle (S) morphologies of PS-*b*-PEO/[EMIM][Tf_2N] with either the IL distributed in the PEO phase (IL-PEO) or forming a separate microphase (IL-Micro) at the PS/PEO block size ratios of (a) 1:1, (b) 4:5, (c) 1:2, (d) 2:1, (e) 1:4, (f) 7:2, (g) 5:4, (h) 7:1, and (i) 1:8 at different IL loadings (<50 vol.%). For clarity, the morphologies are presented for the copolymer/IL (top), copolymer only (middle), and IL only (bottom). Color codes: blue: PS, red: PEO, gray: [EMIM] cation, and green: [Tf_2N] anion.

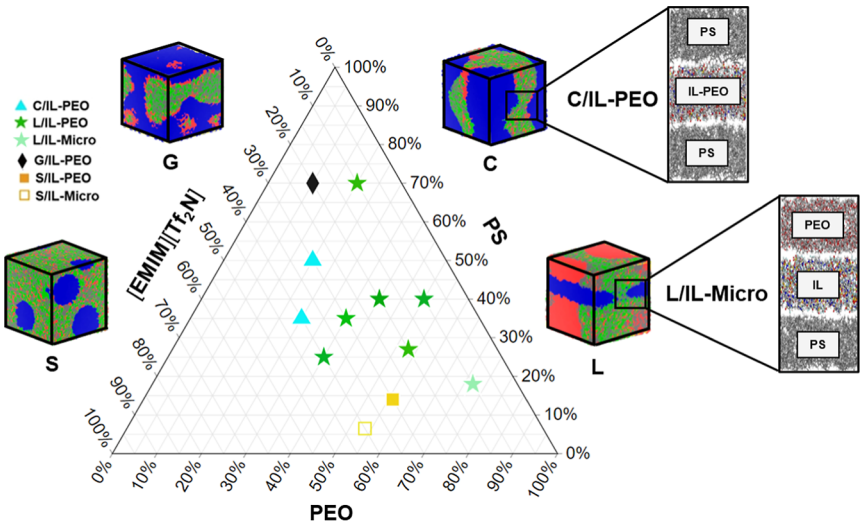

Figure 8. Ternary phase diagram of PS-*b*-PEO/[EMIM][Tf_2N] at 298 K and IL loadings below 50 vol.%. The morphologies are designated as C: cylindrical, L: lamellar, G: gyroid, and S: spherical micelle. The two possible IL distributions in the copolymer, i.e., IL distributed in the PEO phase (IL-PEO) or IL forming a separate microphase (IL-Micro), are shown in the representative zoomed-in phase boundary regions.

$$S^{S}_{CO_2/CH_4} = \frac{\left(\frac{x_{CO_2}}{x_{CH_4}}\right)_{membrane}}{\left(\frac{y_{CO_2}}{y_{CH_4}}\right)_{reservoir}} \quad (10)$$

where y_{CO_2} and y_{CH_4} are the mole fractions of the gas molecules in the reservoir. Permselectivities were calculated next by multiplying the diffusivity selectivities by the solubility selectivities from the following equation

$$S^{P}_{CO_2/CH_4} = S^{D}_{CO_2/CH_4} \times S^{S}_{CO_2/CH_4} \quad (11)$$

https://doi.org/10.1021/acsami.4c21064
ACS Appl. Mater. Interfaces 2025, 17, 11348−11361

RESULTS AND DISCUSSION

Mesoscale Morphologies of the Copolymer/IL Systems. The equilibrium morphologies of the 12 PS-*b*-PEO/[EMIM][Tf_2N] systems (Figure 3) at IL loadings below 50% and different PS/PEO block size ratios are provided in Figure 7. These morphologies are also identified in the ternary phase diagram shown in Figure 8.

By investigating the equilibrium morphologies of PS-*b*-PEO/[EMIM][Tf_2N] in Figure 8, the L, C, or S morphologies are observed to result from IL loadings below 50 vol.%, with the L morphology being the dominant one. Interestingly, similar morphologies are observed for PS-*b*-PEO/[EMIM][SCN] (Figure 3a).[6] A one-to-one comparison between the morphologies of these two copolymer/IL systems is shown in Table 4.

Table 4. Morphologies of the PS-*b*-PEO/[EMIM][Tf_2N] and PS-*b*-PEO/[EMIM][SCN] Systems at Corresponding PS/PEO Block Size Ratios and IL Loadings[b]

coarse-grained chain topology	coarse-grained block size ratio	IL loading (vol.%)	PS-*b*-PEO/[EMIM][Tf_2N] morphology	PS-*b*-PEO/[EMIM][SCN] morphology[a]
PS20- PEO20	**1:1**	**20**	**L/IL-PEO ⟷ L/IL-PEO**	
PS20- PEO20	**1:1**	**30**	**L/IL-PEO ⟷ L/IL-PEO**	
PS20- PEO25	**4:5**	**10**	**L/IL-PEO ⟷ L/IL-PEO**	
PS20- PEO25	4:5	40	L/IL-PEO	C/IL-PEO
PS10- PEO20	1:2	20	L/IL-PEO	C/IL-PEO
PS20- PEO10	2:1	30	C/IL-PEO	L/IL-PEO
PS10- PEO40	1:4	10	L/IL-Micro	C/IL-Micro
PS10- PEO40	1:4	30	S/IL-PEO	G/IL-Micro
PS14- PEO4	**7:2**	**10**	**L/IL-PEO ⟷ L/IL-PEO**	
PS25- PEO20	**5:4**	**40**	**C/IL-PEO ⟷ C/IL-PEO**	
PS14- PEO2	**7:1**	**20**	**G/IL-PEO ⟷ G/IL-PEO**	
PS5- PEO40	1:8	40	S/IL-Micro	G/IL-PEO

[a]From ref 6. [b]Note: Rows in bold font identify matching morphologies between the two systems.

With respect to the IL distribution in the systems, the dominant one is that of IL-PEO (83% of the cases), followed by IL-Micro (17% of the cases). Also, half of the copolymer/IL configurations resulted in similar morphologies (Table 4). The mismatch in the rest of the morphologies may be attributed to the differences in the miscibility of the interacting beads, which are associated with their Flory–Huggins interaction parameters (Table 2). Overall, the two copolymer/IL systems provide favorable L and C morphologies at the selected copolymer block size ratios and IL loadings of <50 vol.% (Figure 7). To gain molecular insights into the effect of IL nanoconfinement in the copolymer/IL systems on the CO_2/CH_4 gas transport properties, the PS, PEO, and IL phase boundaries in the L/IL-PEO, L/IL-Micro, C/IL-PEO, and C/IL-Micro systems (zoomed-in regions in Figure 8) are explored next.

Molecular Gas Transport in the Copolymer/IL Phase Boundaries. *Component Distributions in the Equilibrated Systems.* The equilibrium density profiles of the copolymer/IL components (PS, PEO, [EMIM][SCN], and [EMIM][Tf_2N]) in the nanoconfined IL systems (Figure 4) are shown in Figure 9 for the two confinement lengths of 2.5 and 5 nm. Overall, it is observed that both [EMIM][SCN] and [EMIM][Tf_2N] remain in their IL-PEO or IL-Micro confined phases at equilibrium, though some diffusion of the ILs into the neighboring PS or PEO phases occur. A shift is observed in the interface, particularly on the PEO side in Figure 9e–h, which can be attributed to the interdiffusion of the ILs into the polymer domains. This effect is especially pronounced for [EMIM][Tf_2N] at both confinement lengths (Figure 9g,h), reflecting a greater degree of miscibility between this IL and PEO. The displacement of the PEO-IL interface toward the IL phase suggests that PEO chains are penetrating into the IL-rich region, likely driven by favorable interactions between the ether oxygen atoms of PEO and the IL. Additionally, in Figure 9e,f, unique density profiles are observed with the IL distribution becoming symmetric as the confinement length increases (Figure 9f). This is evidence of strong compatibility between [EMIM][Tf_2N] and PEO. The increase in confinement length seems to facilitate spatial distribution of the IL components and reduce the influence of neighboring polymer domains. The result is a uniform IL redistribution that minimizes the free energy of the system.

Gas Diffusivities. The MSD plots of CO_2 and CH_4 in the bulk polymers and IL systems at two system sizes of $10 \times 10 \times 2.5$ and $10 \times 10 \times 5$ nm^3 are shown in Figure 10. The MSD plots provide a visual representation of how far molecules move on average over time. They show the relationship between the average squared displacement of a molecular species and the time elapsed. Overall, the MSD of both CO_2 and CH_4 in bulk ILs are observed to be significantly larger than those of bulk PEO and bulk PS, as expected. Also, the MSD of CH_4 in the bulk ILs is lower than that of CO_2, which implies these ILs have potential for CO_2/CH_4 separation. The MSD values of the bulk systems follow the order of bulk [EMIM][Tf_2N] > bulk [EMIM][SCN] > bulk PEO > bulk PS. Furthermore, the system size is found to have no appreciable effect on the MSD of CO_2 and CH_4 in bulk polymers or ILs.

The MSD plots of CO_2 and CH_4 in the nanoconfined IL and PS/PEO/PS (control) systems at the two confinement lengths of 2.5 and 5 nm are shown in Figure 11. Overall, the IL-Micro morphology, i.e., PS/[EMIM][SCN]/PEO and PS/[EMIM][Tf_2N]/PEO exhibited the largest MSD values of CO_2 and CH_4 at or near equilibrium and both confinement lengths. In the case of the PS-*b*-PEO/[EMIM][SCN] system (Figure 11a,b), the IL-PEO morphology, i.e., PS/[EMIM][SCN]-PEO/PS, exhibited the lowest average MSD values of CO_2 and CH_4 at both confinement lengths, while the MSD curve of the PS/PEO/PS control system morphology, fell in between the two. In the case of the PS-*b*-PEO/[EMIM][Tf_2N] system (Figure 11c,d), a similar behavior is observed, except for IL-PEO morphology, i.e., PS/[EMIM][Tf_2N]-PEO/PS, at the confinement length of 2.5 nm. Additionally, the IL-Micro morphology, i.e., PS/[EMIM][Tf_2N]/PEO, yield higher average MSD values of CO_2 and CH_4 than those of PS/[EMIM][SCN]/PEO at both confinement lengths. In general, these results suggest that in the phase boundary regions of the copolymer/IL systems, where the IL is nanoconfined between the PS and PEO phases, the mobility of both CO_2 and CH_4 are enhanced compared to when the IL is distributed in the PEO phase (IL-PEO) and nanoconfined between the PS phases (Figure 11). Also, on average, the PS-nanoconfined [EMIM][Tf_2N] systems (Figure 11c,d) provided more CO_2 and CH_4 mobility than PS-nanoconfined [EMIM][SCN] systems. It should be mentioned here that these results only apply to the phase boundary regions and do not necessarily scale up to the gas separation performance of the copolymer/IL membranes. Another observation from Figure 11 is the confinement length effect on the CO_2 and CH_4 mobility in the nanoconfined IL regions. Overall, the CO_2 and CH_4 mobilities increase with increasing confinement length, although the increase is not necessarily linear. The confinement length effect will be more evident when gas diffusivities are calculated next. Moreover, the relative gas transport efficiencies of the

https://doi.org/10.1021/acsami.4c21064
ACS Appl. Mater. Interfaces 2025, 17, 11348–11361

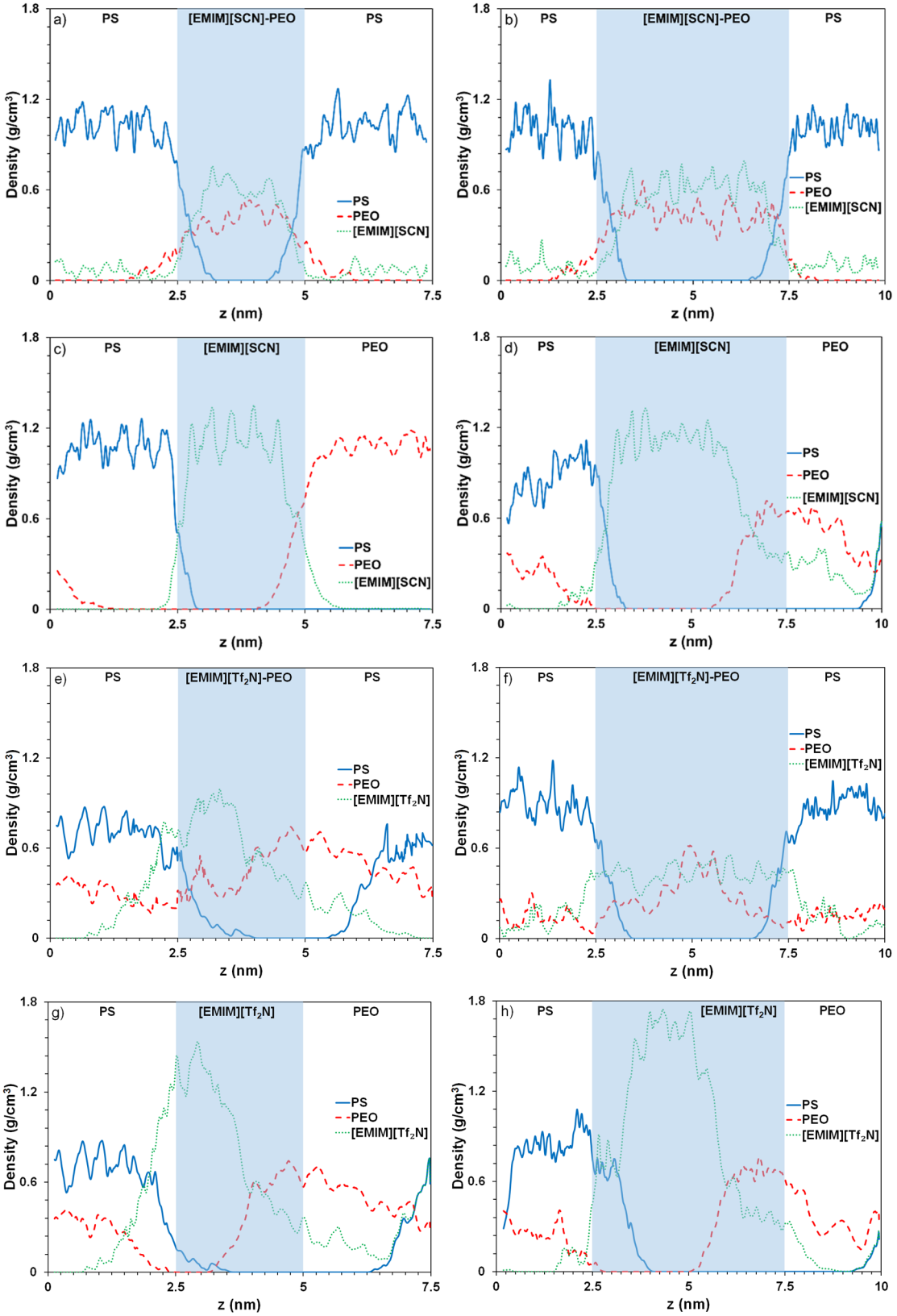

Figure 9. Equilibrium density profiles of the components of the copolymer/IL systems (polymers and ILs) in the PS/IL and PEO/IL phase boundaries: (a,b) PS/[EMIM][SCN]-PEO/PS at confinement lengths of 2.5 and 5 nm, respectively, (c,d) PS/[EMIM][SCN]/PEO at confinement lengths of 2.5 and 5 nm, respectively, (e, f) PS/[EMIM][Tf_2N]-PEO/PS at confinement lengths of 2.5 and 5 nm, respectively, and (g,h) PS/[EMIM][Tf_2N]/PEO at confinement lengths of 2.5 and 5 nm, respectively. The blue-shaded regions represent the IL-PEO or IL-Micro confinement regions within the phase boundaries.

https://doi.org/10.1021/acsami.4c21064
ACS Appl. Mater. Interfaces 2025, 17, 11348−11361

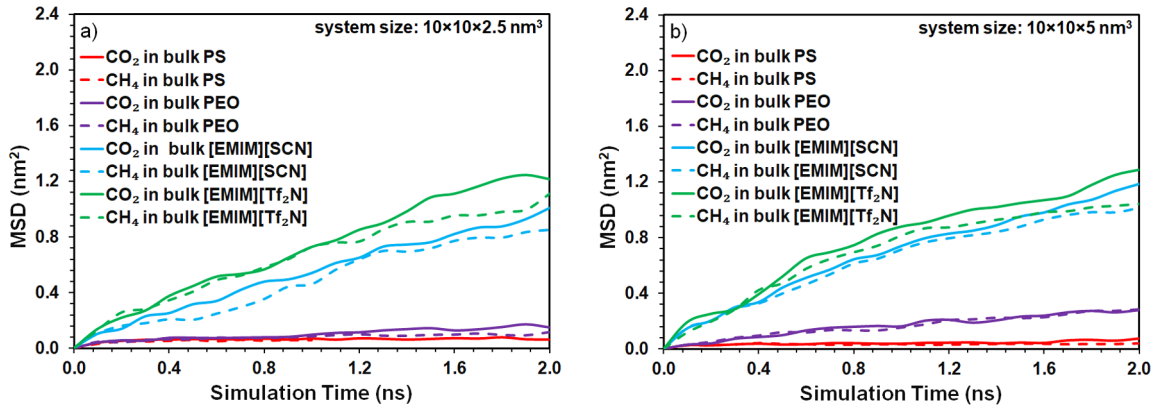

Figure 10. MSD plots of CO_2 and CH_4 in bulk PS, bulk PEO, [EMIM][SCN], and [EMIM][Tf_2N] at the system size of (a) $10 \times 10 \times 2.5$ nm^3 and (b) $10 \times 10 \times 5$ nm^3.

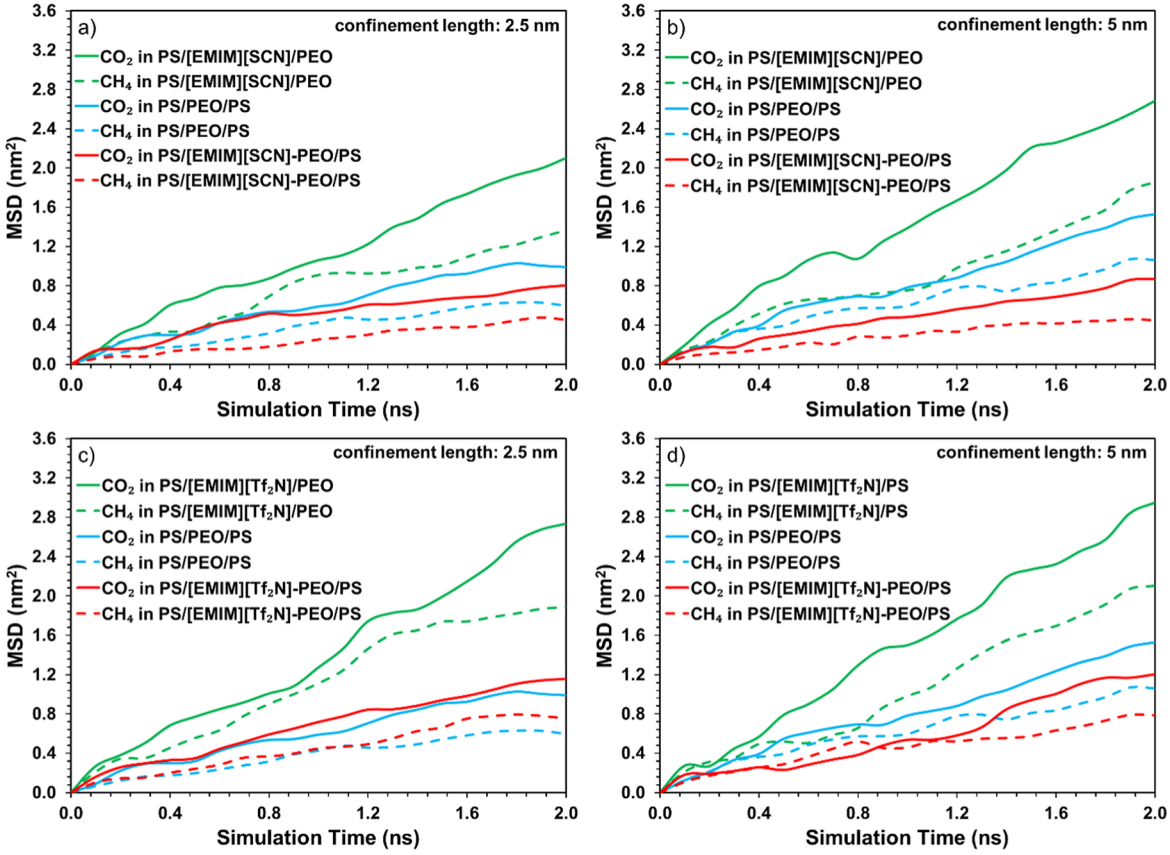

Figure 11. (a,b) MSD plots of CO_2 and CH_4 in PS/[EMIM][SCN]/PEO, PS/PEO/PS (control), and PS/[EMIM][SCN]-PEO/PS systems at two confinement lengths of 2.5 and 5 nm, respectively; (c,d) MSD plots of CO_2 and CH_4 in PS/[EMIM][Tf_2N]/PEO, PS/PEO/PS (control), and PS/[EMIM][Tf_2N]-PEO/PS systems at two confinement lengths of 2.5 and 5 nm, respectively.

nanoconfined IL versus the bulk systems become apparent as the solubility, diffusivity, and permselectivities are discussed in later sections.

The gas diffusivities obtained by linear fits to the MSD plots (Figures 10 and 11) indicate some dependence on system size. Overall, the self-diffusivity of a chemical species at infinite system size (D_∞) can be determined from the equation proposed by Yeh and Hummer[57]

$$D_\infty = D_L + \frac{K_B T \xi}{6\pi\eta L} \quad (12)$$

where D_L is the self-diffusivity for a cell size of L, K_B is the Boltzmann constant, $\xi = 2.837298$ for a cubic system, and η is viscosity. In Table 5, the infinite diffusivities of CO_2 for the two system sizes of $10 \times 10 \times 2.5$ and $10 \times 10 \times 5$ nm^3, as well as their relative differences at 298 K are provided. Overall, the differences range from 6 to 13%, which are within acceptable limits for MD simulations. In general, the gas diffusivity calculations herein are reasonably accurate and reliable, with minor sensitivities to system size.

The diffusivities of CO_2 and CH_4 in the bulk and nanoconfined IL systems (in the order of 10^{-10} m^2/s) at the confinement lengths of 2.5 and 5 nm are listed in Table 6 in the

https://doi.org/10.1021/acsami.4c21064
ACS Appl. Mater. Interfaces 2025, 17, 11348−11361

Table 5. Infinite Diffusivities (D_∞) of CO_2 and CH_4 in the Bulk Systems at 298 K for the System Sizes of 10 × 10 × 2.5 and 10 × 10 × 5 nm^3

system	D_∞ of CO_2 ($\times 10^{-10}$ m^2/s) system size		difference (%)
	10 × 10 × 2.5 nm^3	10 × 10 × 5 nm^3	
bulk PS	1.18	1.34	13
bulk PEO	1.45	1.55	6
bulk [EMIM][SCN]	3.37	3.68	9
bulk [EMIM][Tf_2N]	5.05	5.70	12

Table 6. Diffusivities (D) of CO_2 and CH_4 in the Bulk and Nanoconfined IL Systems at 298 K for the Confinement Lengths of 2.5 and 5 nm

system	D ($\times 10^{-10}$ m^2/s) confinement length: 2.5 nm		confinement length: 5 nm	
	CO_2	CH_4	CO_2	CH_4
Bulk PS[a]	1.18	1.10	1.34	1.29
Bulk PEO[a]	1.45	1.59	1.55	1.34
PS/PEO/PS	2.87	2.25	3.05	3.18
PS/[EMIM][SCN]-PEO/PS	3.32	3.00	3.60	2.53
Bulk [EMIM][SCN][a]	3.37	3.10	3.68	3.50
PS/[EMIM][Tf_2N]-PEO/PS	4.13	3.72	4.45	3.43
PS/[EMIM][SCN]/PEO	4.47	3.98	4.93	3.94
Bulk [EMIM][Tf_2N][a]	5.05	4.65	5.70	4.82
PS/[EMIM][Tf_2N]/PEO	6.00	5.77	7.37	5.37

[a]With respect to the bulk systems, the confinement lengths of 2.5 and 5 nm refer to the system sizes of 10 × 10 × 2.5 and 10 × 10 × 5 nm^3, respectively.

ascending order of CO_2 diffusivity. Earlier reports indicate the diffusivities of CO_2 and CH_4 in the bulk PEO,[58] bulk PS,[59] and bulk ILs ranging from 10^{-11} to 10^{-10} m^2/s, depending on the polymer and IL type, pressure, and temperature.[19] The lowest and highest CO_2 diffusivity is observed for the bulk PS and PS/[EMIM][Tf_2N]/PEO system, respectively, at both IL confinement lengths (Table 6), with the latter being about 5−6 times higher than the former. With respect to the CO_2 diffusion in bulk ILs, the higher CO_2 diffusivity is observed for the bulk [EMIM][Tf_2N], i.e., $6.00 \times 10^{-10} - 7.37 \times 10^{-10}$ m^2/s (Table 6), which is in close agreement with the experimental value of 6.6×10^{-10} m^2/s reported by Scovazzo et al.[60] As expected, the CO_2 and CH_4 diffusivities in the bulk system follow the order of bulk PS < bulk PEO < [EMIM][SCN] < [EMIM][Tf_2N] at both confinement lengths (Table 6). Interestingly, the nanoconfinement of PEO between the PS phases leads to an increase in the CO_2 and CH_4 diffusivities in the PEO phase by a factor of 2 (Table 6).When the IL is nanoconfined between the PS and PEO phases, the CO_2 diffusivities in the confined IL regions are higher for [EMIM]-[Tf_2N] than [EMIM][SCN] by about 35−50%, depending on the confinement length (Table 6). Finally, when the IL is distributed in the PEO phase and confined between the PS phases, the CO_2 diffusivities in the confined IL regions are slightly smaller for [EMIM][SCN]-PEO than [EMIM][Tf_2N]-PEO (Table 6). Overall, [EMIM][Tf_2N] is found to affect both CO_2 and CH_4 diffusion more profoundly when nanoconfined between the polymer phases (either as a separate phase or distributed in the PEO phase) than [EMIM][SCN]. These observations are generally associated with enhanced molecular interactions in the nanoconfined IL-PEO or IL-Micro regions, originating from the electrostatic interactions between the ion pairs and structural organization within the nanoconfined spaces, both of which promote diffusion pathways and gas mobility. Additionally, the presence of interface promotes the increase of free volume and alters molecular packing at the phase boundaries. This structural reorganization may depress viscosity and create additional diffusion sites.[61] Therefore, molecular transport within the nanoconfined regions is facilitated. Literature suggests that IL microphase separation can reduce viscosity, facilitating easier molecular transport.[62] Therefore, higher CO_2 diffusivity agrees with the findings herein.

With respect to the CH_4 diffusivities in the different systems, similar trends are observed to those of CO_2 diffusivities at both confinement lengths (Table 6).

Gas Solubilities. The solubilities of CO_2 and CH_4 in the bulk and nanoconfined IL systems are listed in Table 7 in the ascending order of CO_2 solubility in the confinement length of 2.5 nm. For some systems such as bulk ILs, there is a noticeable effect of system size on gas solubility (Table 7). Overall, the calculated average CO_2 solubilities (mol/mol) in the bulk systems (~0.009−0.036) are comparable to the reported CO_2 solubilities in literature for the relevant systems. For example, Makino et al.[63] reported a CO_2 solubility of ~0.22 (mol/mol) in [EMIM][Tf_2N] at 298 K and 1 MPa, while Schilderman et al.[64] reported a value of ~0.12 at 314 K and 0.5 MPa. Although there is no temperature and pressure equivalence in these reports, these values may roughly be compared to the calculated CO_2 diffusivity of ~0.05 in [EMIM][Tf_2N] in this work (Table 7). Also, Sato et al.[59] reported a value of ~0.005 (mol/mol) for the solubility of CO_2 in PS at 314 K and 0.19 MPa, which may roughly be compared to the CO_2 solubility of ~0.008 in PS, as calculated herein (Table 7). Huang and Peng[65] reported a CO_2 solubility of ~0.006 in [EMIM][SCN] at 298 K and 105 kPa, which is smaller than the corresponding value calculated in this work, i.e., ~0.034 (Table 7).

Table 7. Solubilities of CO_2 and CH_4 in the Bulk and Nanoconfined IL Systems at 298 K for the Confinement Lengths of 2.5 and 5 nm

system	confinement length: 2.5 nm		confinement length: 5 nm	
	CO_2	CH_4	CO_2	CH_4
Bulk PS[a]	0.009	0.003	0.008	0.002
Bulk PEO[a]	0.009	0.002	0.011	0.002
PS/PEO/PS	0.011	0.002	0.012	0.002
Bulk [EMIM][SCN][a]	0.025	0.004	0.034	0.005
PS/[EMIM][SCN]-PEO/PS	0.031	0.004	0.032	0.003
PS/[EMIM][Tf_2N]-PEO/PS	0.034	0.003	0.036	0.003
Bulk [EMIM][Tf_2N][a]	0.036	0.005	0.052	0.007
PS/[EMIM][SCN]/PEO	0.079	0.006	0.112	0.007
PS/[EMIM][Tf_2N]/PEO	0.198	0.016	0.270	0.013

[a]With respect to the bulk systems, the confinement lengths of 2.5 and 5 nm refer to the system sizes of 10 × 10 × 2.5 and 10 × 10 × 5 nm^3, respectively.

Overall, the CO_2 solubilities in the IL-Micro morphologies, i.e., the IL nanoconfined between the PS and PEO phases, were significantly higher than the corresponding bulk ILs at both confinement lengths (Table 7). In fact, the PS/[EMIM][Tf_2N]/PEO system exhibited the highest CO_2 solubility (0.270), followed by the PS/[EMIM][SCN]/PEO system (0.112) at the confinement length of 5 nm. However, when the IL is distributed in the PEO phase and nanoconfined between the PS phases (IL-PEO morphologies), the CO_2 solubilities are not necessarily enhanced over the bulk ILs (Table 7).

Gas Selectivities. The solubility selectivities ($S^S_{CO_2/CH_4}$), diffusivity selectivities ($S^D_{CO_2/CH_4}$), and permselectivities ($S^P_{CO_2/CH_4}$) of the bulk and nanoconfined IL systems are reported

https://doi.org/10.1021/acsami.4c21064
ACS Appl. Mater. Interfaces 2025, 17, 11348−11361

Table 8. Solubility Selectivities ($S^S_{CO_2/CH_4}$), Diffusivity Selectivities ($S^D_{CO_2/CH_4}$), and Permselectivities ($S^P_{CO_2/CH_4}$) of the Bulk and Nanoconfined IL Systems at 298 K for the Confinement Lengths of 2.5 and 5 nm

system	confinement length: 2.5 nm			confinement length: 5 nm		
	$S^S_{CO2/CH4}$	$S^D_{CO2/CH4}$	$S^P_{CO2/CH4}$	$S^S_{CO2/CH4}$	$S^D_{CO2/CH4}$	$S^P_{CO2/CH4}$
Bulk PS[a]	3.0	1.1	3.3	4.0	1.0	4.0
Bulk PEO[a]	4.5	0.9	4.0	5.5	1.1	6.0
PS/PEO/PS	5.5	1.2	6.6	6.0	0.9	5.4
Bulk [EMIM][SCN][a]	6.2	1.1	6.8	6.8	1.0	6.8
Bulk [EMIM][Tf_2N][a]	7.2	1.0	7.2	7.4	1.2	8.8
PS/[EMIM][SCN]-PEO/PS	7.7	1.1	8.4	10.6	1.4	14.8
PS/[EMIM][Tf_2N]-PEO/PS	11.3	1.1	12.4	12.6	1.3	16.3
PS/[EMIM][SCN]/PEO	13.1	1.1	14.4	16.0	1.2	19.2
PS/[EMIM][Tf_2N]/PEO	12.3	1.1	13.5	20.7	1.3	26.9

[a]With respect to the bulk systems, the confinement lengths of 2.5 and 5 nm refer to the system sizes of 10 × 10 × 2.5 and 10 × 10 × 5 nm^3, respectively.

in Table 8, in the ascending order of permselectivities for the confinement length of 5 nm. The calculated CO_2/CH_4 solubility selectivity of the bulk [EMIM][Tf_2N], i.e., 7.2−7.4 in Table 8, may be compared to the ideal selectivity of 7.8 reported by Chen et al.[66] and 11.2 reported by Finotello et al.[67] Overall, the highest mixed-gas CO_2/CH_4 solubility selectivities and permselectivities are observed for nanoconfined [EMIM][Tf_2N], i.e., PS/[EMIM][Tf_2N]/PEO at the confinement length of 5 nm, followed by nanoconfined [EMIM][SCN], i.e., PS/[EMIM]-[SCN]/PEO at the same confinement length (Table 8). The mixed-gas CO_2/CH_4 permselectivities of the nanoconfined IL systems are, on average, larger than the corresponding bulk ILs by 3-fold (Table 8). Based on the selectivities obtained herein for the nanoconfined IL systems, CO_2/CH_4 separation in PS/[EMIM][Tf_2N]/PEO is found to be better than the other nanoconfined IL or bulk systems (Table 8). Interestingly, the gas selectivities increase with increasing confinement length, suggesting that there should be an optimal (or critical) confinement length for a given IL, where the gas selectivities are maximum. It is expected that the gas selectivities approach the bulk values beyond this critical confinement length. Interfaces in nanoconfined systems are believed to act as active sites, where gas molecules can effectively interact with the IL components on one side and the confining polymer on the other side. Thus, enhancement in selectivity can be explained by the preferential interaction of CO_2 with the interfacial regions, while CH_4 seems to exhibit less favorable interactions.[68] It is also important to note that the extent of favorable interactions depends on various factors, including the nature of the confining material, the type of IL, and the degree of nanoconfinement. For example, the results herein demonstrate that [EMIM][Tf_2N] exhibits a more pronounced enhancement in CO_2 selectivity when nanoconfined between the PS and PEO phases than [EMIM][SCN]. Overall, these findings highlight the critical role of interfaces in nanoconfined IL systems for gas separation applications. By carefully engineering the interfacial properties and confinement dimensions, it may be possible to further optimize the performance of these materials for specific gas separations.

CONCLUSIONS

A combined mesoscopic dynamics simulation and hybrid grand canonical Monte Carlo-molecular dynamics (GCMC-MD) simulations revealed the morphologies and CO_2/CH_4 separation performances of PS-*b*-PEO/[EMIM][SCN] and PS-*b*-PEO/[EMIM][Tf_2N] membranes. At least for half of the investigated cases, the two diblock copolymer/IL systems yielded similar lamellar (L) and cylindrical (C) copolymer morphologies with the IL distributed in the PEO phase (IL-PEO) or forming a separate microphase (IL-Micro) at comparable PS/PEO block size ratios and IL loadings (<50 vol %). These findings suggest that, although the two ILs have different Kamlet−Taft solvent parameters, the desirable L or C morphologies for CO_2/CH_4 separation can be achieved for both PS-*b*-PEO/IL membranes at IL loadings <50 vol % with the same PS-*b*-PEO copolymer specifications.

At the phase boundary regions of the nanoconfined IL (PS/IL/PEO) or nanoconfined IL-PEO (PS/IL-PEO/PS) systems, the CO_2/CH_4 gas transport and separation properties were found to be different than regions dominated by neat PS, PEO, or ILs (modeled as bulk systems). Also, there was an appreciable confinement size effect on the gas transport properties. In particular, the CO_2/CH_4 permselectivities of the nanoconfined [EMIM][SCN], i.e., PS/[EMIM][SCN]/PEO, and [EMIM]-[Tf_2N], i.e., PS/[EMIM][Tf_2N]/PEO were nearly three times higher than those of the bulk IL systems, suggesting that the IL-Micro phases promote better CO_2/CH_4 separation. The gas transport and separation performance were further enhanced by an increase in the confinement length, suggesting that there might be an optimal (or critical) IL confinement length, after which the system behaves similarly to the bulk ILs. In general, the IL nanoconfinement was found to be a viable strategy to improve the gas transport and separation performance in copolymer/IL membranes.

AUTHOR INFORMATION

Corresponding Author

Sasan Nouranian − *Department of Chemical Engineering, University of Mississippi, Oxford, Mississippi 38677, United States; Center for Graphene Research and Innovation, University of Mississippi, Oxford, Mississippi 38677, United States;* orcid.org/0000-0002-8319-2786; Email: sasan@olemiss.edu

Authors

Azam Salmankhani − *Department of Chemical Engineering, University of Mississippi, Oxford, Mississippi 38677, United States*

Alexander M. Lopez − *Department of Chemical Engineering, University of Mississippi, Oxford, Mississippi 38677, United States;* Present Address: Department of Mathematics & Physical Sciences, Rogers State University, Claremore, OK 74017; orcid.org/0000-0001-9810-3902

https://doi.org/10.1021/acsami.4c21064
ACS Appl. Mater. Interfaces 2025, 17, 11348−11361

Paul Scovazzo − *Department of Chemical Engineering, University of Mississippi, Oxford, Mississippi 38677, United States;* orcid.org/0000-0003-2990-7055

Adam E. Smith − *Department of Chemical Engineering, University of Mississippi, Oxford, Mississippi 38677, United States; Department of Biomedical Engineering, University of Mississippi, Oxford, Mississippi 38677, United States;* orcid.org/0000-0003-1733-443X

Complete contact information is available at: https://pubs.acs.org/10.1021/acsami.4c21064

Notes

The authors declare no competing financial interest.

■ ACKNOWLEDGMENTS

This material is based upon work supported by the National Science Foundation under Grant no. CBET-2031021.

■ REFERENCES

(1) Nunes, S. P. Chapter 11—Block Copolymer Membranes. In *Sustainable Nanoscale Engineering*; Szekely, G., Livingston, A., Eds.; Elsevier, 2020; pp 297−316.

(2) Hossain, I.; Nam, S. Y.; Rizzuto, C.; Barbieri, G.; Tocci, E.; Kim, T.-H. PIM-Polyimide Multiblock Copolymer-based Membranes with Enhanced CO_2 Separation Performances. *J. Membr. Sci.* **2019**, *574*, 270−281.

(3) Rynkowska, E.; Fatyeyeva, K.; Kujawski, W. Application of Polymer-Based Membranes Containing Ionic Liquids in Membrane Separation Processes: A Critical Review. *Rev. Chem. Eng* **2017**, *34* (3), 341−363.

(4) Dai, Z.; Noble, R. D.; Gin, D. L.; Zhang, X.; Deng, L. Combination of Ionic Liquids with Membrane Technology: A New Approach for CO_2 Separation. *J. Membr. Sci.* **2016**, *497*, 1−20.

(5) Mai, Y.; Eisenberg, A. Self-Assembly of Block Copolymers. *Chem. Soc. Rev.* **2012**, *41* (18), 5969−5985.

(6) Salmankhani, A.; Scovazzo, P.; Lopez, A. M.; Smith, A. E.; Nouranian, S. Self-Assembled Morphologies of Polystyrene-*block*-poly(ethylene oxide)/1-Ethyl-3-methylimidazolium Thiocyanate Membranes by Mesoscopic Dynamics Simulation. *Macromolecules* **2023**, *56* (17), 7153−7165.

(7) Adzima, B. J.; Venna, S. R.; Klara, S. S.; He, H.; Zhong, M.; Luebke, D. R.; Mauter, M. S.; Matyjaszewski, K.; Nulwala, H. B. Modular Polymerized Ionic Liquid Block Copolymer Membranes for CO_2/N_2 Separation. *J. Mater. Chem. A* **2014**, *2* (21), 7967−7972.

(8) Zeeshan, M.; Keskin, S.; Uzun, A. Enhancing CO_2/CH_4 and CO_2/N_2 Separation Performances of ZIF-8 by Post-Synthesis Modification with [BMIM][SCN]. *Polyhedron* **2018**, *155*, 485−492.

(9) Wijayasekara, D. B.; Cowan, M. G.; Lewis, J. T.; Gin, D. L.; Noble, R. D.; Bailey, T. S. Elastic Free-Standing RTIL Composite Membranes for CO_2/N_2 Separation Based on Sphere-Forming Triblock/Diblock Copolymer Blends. *J. Membr. Sci.* **2016**, *511*, 170−179.

(10) Zhang, S.; Zhang, J.; Zhang, Y.; Deng, Y. Nanoconfined Ionic Liquids. *Chem. Rev.* **2017**, *117* (10), 6755−6833.

(11) Yasmeen, I.; Ilyas, A.; Shamair, Z.; Gilani, M. A.; Rafiq, S.; Bilad, M. R.; Khan, A. L. Synergistic Effects of Highly Selective Ionic Liquid Confined in Nanocages: Exploiting the Three Component Mixed Matrix Membranes for CO_2 Capture. *Chem. Eng. Res. Des.* **2020**, *155*, 123−132.

(12) Jomekian, A.; Bazooyar, B.; Behbahani, R. M.; Mohammadi, T.; Kargari, A. Ionic Liquid-Modified Pebax® 1657 Membrane Filled by ZIF-8 Particles for Separation of CO_2 from CH_4, N_2 and H_2. *J. Membr. Sci.* **2017**, *524*, 652−662.

(13) Bandegi, A.; Marquez Garcia, M.; Banuelos, J. L.; Firestone, M. A.; Foudazi, R. Soft Nanoconfinement of Ionic Liquids in Lyotropic Liquid Crystals. *Soft Matter* **2021**, *17*, 8118−8129.

(14) Harmanli, I.; Tarakina, N. V.; Antonietti, M.; Oschatz, M. Giant" Nitrogen Uptake in Ionic Liquids Confined in Carbon Pores. *J. Am. Chem. Soc.* **2021**, *143*, 9377−9384.

(15) Borghi, F.; Podestà, A. Ionic Liquids under Nanoscale Confinement. *Adv. Phys.:X* **2020**, *5* (1), 1736949.

(16) Shah Buddin, M. M. H.; Ahmad, A. L. Performance Evaluation of Supported Ionic Liquid Membranes (SILMs) Derived from Optimized PES/PDMS/ZIF-L Composites for CO_2 Separation. *Ind. Eng. Chem. Res.* **2023**, *62*, 5199−5215.

(17) Otero-Lema, M.; Lois-Cuns, R.; Martínez-Crespo, P.; Rivera-Pousa, A.; Montes-Campos, H.; Méndez-Morales, T.; Varela, L. M. On the Molecular Mechanisms of H_2/N_2 Uptake in Confined Ionic Liquids: A Computational Study. *J. Mol. Liq.* **2024**, *405*, 124909.

(18) Wang, Y.; Niu, Z.; Dai, Y.; Zhong, S.; Li, J. Efficient CO2 Separation by Ionic Liquid Nanoconfined in Ultra-Thin TCOH@ Pebax-1657 MMM. *Sep. Purif. Technol.* **2023**, *325*, 124667.

(19) Rahmani, F.; Scovazzo, P.; Pasquinelli, M.; Nouranian, S. Effects of Ionic Liquid Nanoconfinement on the CO_2/CH_4 Separation in Poly(vinylidene fluoride)/1-Ethyl-3-methyl-Imidazolium Thiocyanate Membranes. *ACS Appl. Mater. Interfaces* **2021**, *13*, 44460−44469.

(20) Chen, D.; Ying, W.; Guo, Y.; Ying, Y.; Peng, X. Enhanced Gas Separation through Nanoconfined Ionic Liquid in Laminated MoS_2 Membrane. *ACS Appl. Mater. Interfaces* **2017**, *9* (50), 44251−44257.

(21) Tian, Z.; Dai, S.; Jiang, D. Confined Ionic Liquid in an Ionic Porous Aromatic Framework for Gas Separation. *ACS Appl. Polym. Mater.* **2019**, *1*, 95.

(22) Tan, M.; Lu, J.; Zhang, Y.; Jiang, H. Ionic Liquid Confined in Mesoporous Polymer Membrane with Improved Stability for CO_2/N_2 Separation. *Nanomaterials* **2017**, *7* (10), 299.

(23) Min, H. J.; Kim, Y. J.; Kang, M.; Seo, C.-H.; Kim, J.-H.; Kim, J. H. Crystalline Elastomeric Block Copolymer/Ionic Liquid Membranes with Enhanced Mechanical Strength and Gas Separation Properties. *J. Membr. Sci.* **2022**, *660*, 120837.

(24) Grünauer, J.; Shishatskiy, S.; Abetz, C.; Abetz, V.; Filiz, V. Ionic Liquids Supported by Isoporous Membranes for CO_2/N_2 Gas Separation Applications. *J. Membr. Sci.* **2015**, *494*, 224−233.

(25) Spange, S.; Lungwitz, R.; Schade, A. Correlation of Molecular Structure and Polarity of Ionic Liquids. *J. Mol. Liq.* **2014**, *192*, 137−143.

(26) Tomé, L. C.; Mecerreyes, D.; Freire, C. S. R.; Rebelo, L. P. N.; Marrucho, I. M. Pyrrolidinium-Based Polymeric Ionic Liquid Materials: New Perspectives for CO_2 Separation Membranes. *J. Membr. Sci.* **2013**, *428*, 260−266.

(27) Scovazzo, P. Determination of the Upper Limits, Benchmarks, and Critical Properties for Gas Separations Using Stabilized Room Temperature Ionic Liquid Membranes (SILMs) for the Purpose of Guiding Future Research. *J. Membr. Sci.* **2009**, *343* (1−2), 199−211.

(28) Khakpay, A.; Scovazzo, P. Reverse-Selective Behavior of Room Temperature Ionic Liquid Based Membranes for Natural Gas Processing. *J. Membr. Sci.* **2018**, *545*, 204−212.

(29) Fraaije, J. G. E. M.; van Vlimmeren, B. A. C.; Maurits, N. M.; Postma, M.; Evers, O. A.; Hoffmann, C.; Altevogt, P.; Goldbeck-Wood, G. The Dynamic Mean-Field Density Functional Method and Its Application to the Mesoscopic Dynamics of Quenched Block Copolymer Melts. *J. Chem. Phys.* **1997**, *106* (10), 4260−4269.

(30) Maurits, N. M.; van Vlimmeren, B. A. C.; Fraaije, J. G. E. M. Mesoscopic Phase Separation Dynamics of Compressible Copolymer Melts. *Phys. Rev. E* **1997**, *56*, 816−825.

(31) Marrink, S. J.; Risselada, H. J.; Yefimov, S.; Tieleman, D. P.; de Vries, A. H. The MARTINI Force Field: Coarse Grained Model for Biomolecular Simulations. *J. Phys. Chem. B* **2007**, *111* (27), 7812−7824.

(32) Zhang, Y.; Fan, X.; Shen, Z.; Zhou, Q. Thermoreversible Ion Gel with Tunable Modulus Self-Assembled by a Liquid Crystalline Triblock Copolymer in Ionic Liquid. *Macromolecules* **2015**, *48*, 4927−4935.

(33) Kusuma, V. A.; Macala, M. K.; Liu, J.; Marti, A. M.; Hirsch, R. J.; Hill, L. J.; Hopkinson, D. Ionic Liquid Compatibility in Polyethylene Oxide/Siloxane Ion Gel Membranes. *J. Membr. Sci.* **2018**, *545*, 292−300.

(34) Gai, Y.; Song, D.-P.; Yavitt, B. M.; Watkins, J. J. Polystyrene-*block*-poly(ethylene oxide) Bottlebrush Block Copolymer Morphology Transitions: Influence of Side Chain Length and Volume Fraction. *Macromolecules* **2017**, *50* (4), 1503−1511.
(35) Sun, H. COMPASS: An Ab Initio Force-Field Optimized for Condensed-Phase Applications-Overview with Details on Alkane and Benzene Compounds. *J. Phys. Chem. B* **1998**, *102* (38), 7338−7364.
(36) Fan, C. F.; Olafson, B. D.; Blanco, M.; Hsu, S. L. Application of Molecular Simulation to Derive Phase Diagrams of Binary Mixtures. *Macromolecules* **1992**, *25*, 3667.
(37) Payne, M. C.; Teter, M. P.; Allan, D. C.; Arias, T. A.; Joannopoulos, J. D. Iterative Minimization Techniques for Ab Initio Total-Energy Calculations: Molecular Dynamics and Conjugate Gradients. *Rev. Mod. Phys.* **1992**, *64* (4), 1045−1097.
(38) Jorgensen, W. L.; Maxwell, D. S.; Tirado-Rives, J. Development and Testing of the OPLS All-Atom Force Field on Conformational Energetics and Properties of Organic Liquids. *J. Am. Chem. Soc.* **1996**, *118* (45), 11225−11236.
(39) Sambasivarao, S. V.; Acevedo, O. Development of OPLS-AA Force Field Parameters for 68 Unique Ionic Liquids. *J. Chem. Theory Comput.* **2009**, *5* (4), 1038−1050.
(40) Dauber-Osguthorpe, P.; Hagler, A. T. Biomolecular Force Fields: Where Have We Been, Where Are We Now, Where Do We Need to Go and How Do We Get There? *J. Comput.-Aided Mol. Des.* **2019**, *33* (2), 133−203.
(41) Pádua, A. A. H.; Costa Gomes, M. F.; Canongia Lopes, J. N. A. Molecular Solutes in Ionic Liquids: A Structural Perspective. *Acc. Chem. Res.* **2007**, *40* (11), 1087−1096.
(42) Zhong, H.; Lai, S.; Wang, J.; Qiu, W.; Lüdemann, H.-D.; Chen, L. Molecular Dynamics Simulation of Transport and Structural Properties of CO_2 Using Different Molecular Models. *J. Chem. Eng. Data* **2015**, *60* (8), 2188−2196.
(43) Doan, Q. T.; Keshavarz, A.; Miranda, C. R.; Behrenbruch, P.; Iglauer, S. Molecular Dynamics Simulation of Interfacial Tension of the CO_2-CH_4-Water and H_2-CH_4-Water Systems at the Temperature of 300 and 323 K and Pressure up to 70 MPa. *J. Energy Storage* **2023**, *66*, 107470.
(44) Jorgensen, W. L.; Tirado-Rives, J. Potential Energy Functions for Atomic-Level Simulations of Water and Organic and Biomolecular Systems. *Proc. Natl. Acad. Sci. U.S.A.* **2005**, *102* (19), 6665−6670.
(45) Dodda, L. S.; Vilseck, J. Z.; Tirado-Rives, J.; Jorgensen, W. L. 1.14*CM1A-LBCC: Localized Bond-Charge Corrected CM1A Charges for Condensed-Phase Simulations. *J. Phys. Chem. B* **2017**, *121* (15), 3864−3870.
(46) Dodda, L. S.; Cabeza de Vaca, I.; Tirado-Rives, J.; Jorgensen, W. L. LigParGen Web Server: An Automatic OPLS-AA Parameter Generator for Organic Ligands. *Nucleic Acids Res.* **2017**, *45* (W1), W331−W336.
(47) Evans, D. J.; Holian, B. L. The Nosé-Hoover Thermostat. *J. Chem. Phys.* **1985**, *83* (8), 4069−4074.
(48) Hockney, R. W.; E, J. W. *Computer Simulation Using Particles*, 1st ed.; CRC Press, 1988; p 540.
(49) Tee, L. S.; Gotoh, S.; Stewart, W. E. Molecular Parameters for Normal Fluids. Lennard-Jones 12−6 Potential. *Ind. Eng. Chem. Fundam.* **1966**, *5* (3), 356−363.
(50) Kong, C. L.; Chakrabarty, M. R. Combining Rules for Intermolecular Potential Parameters. III. Application to the Exp 6 Potential. *J. Phys. Chem.* **1973**, *77* (22), 2668−2670.
(51) Wong-ekkabut, J.; Karttunen, M. The Good, the Bad and the User in Soft Matter Simulations. *Biochim. Biophys. Acta, Biomembr.* **2016**, *1858* (10), 2529−2538.
(52) Larriba, M.; Navarro, P.; García, J.; Rodríguez, F. Selective Extraction of Toluene from N-Heptane Using [Emim][SCN] and [Bmim][SCN] Ionic Liquids as Solvents. *J. Chem. Thermodyn.* **2014**, *79*, 266−271.
(53) Iguchi, M.; Hiraga, Y.; Kasuya, K.; Aida, T. M.; Watanabe, M.; Sato, Y.; Smith, R. L. Viscosity and Density of Poly(ethylene glycol) and Its Solution with Carbon Dioxide at 353.2 and 373.2 K at Pressures up to 15 MPa. *J. Supercrit. Fluids* **2015**, *97*, 63−73.
(54) Yang, F.; Wang, B.; Jiao, Y.; Tan, H.; Wang, X. Density and Viscosity of Three Ionic Liquids with 2,2,2-Trifluoroethanol. *J. Chem. Thermodyn.* **2023**, *181*, 107038.
(55) Frenkel, D.; Smit, B. *Understanding Molecular Simulation from Algorithms to Applications*, 2nd ed.; Academic Press, 1996; Vol. *50*.
(56) Mathé, P.; Novak, E. Simple Monte Carlo and the Metropolis Algorithm. *J. Complex* **2007**, *23* (4), 673−696.
(57) Yeh, I.-C.; Hummer, G. System-Size Dependence of Diffusion Coefficients and Viscosities from Molecular Dynamics Simulations with Periodic Boundary Conditions. *J. Phys. Chem. B* **2004**, *108* (40), 15873−15879.
(58) Chen, J.; Warner, M. J.; Sikora, B.; Kiddle, D.; Coverdell, D.; Allam, O.; Kohl, P. A.; Jang, S. S. The Selective Heating Effect of Microwave Irradiation on a Binary Mixture of Water and Polyethylene Oxide: A Molecular Dynamics Simulation Approach. *Phys. Chem. Chem. Phys.* **2023**, *25* (17), 12522−12531.
(59) Sato, Y.; Takikawa, T.; Takishima, S.; Masuoka, H. Solubilities and Diffusion Coefficients of Carbon Dioxide in Poly(vinyl acetate) and Polystyrene. *J. Supercrit. Fluids* **2001**, *19* (2), 187−198.
(60) Morgan, D.; Ferguson, L.; Scovazzo, P. Diffusivities of Gases in Room-Temperature Ionic Liquids: Data and Correlations Obtained Using a Lag-Time Technique. *Ind. Eng. Chem. Res.* **2005**, *44* (13), 4815−4823.
(61) Dong, M.; Zhang, K.; Wan, X.; Fang, Z.; Hu, Y.; Ye, Z.; Wang, Y.; Li, Z.; Peng, X. Enhanced Molecular Transport in Two-Dimensional Nanoconfined Ionic Liquids. *Appl. Mater. Today* **2022**, *27*, 101458.
(62) Ratajczak, P.; Bachetzky, C.; Wang, Z.; Chojnacka, A.; Fulik, N.; Pameté, E.; Pourhosseini, S. E. M.; Brunner, E.; Beguin, F. Mobility and Phase Transitions of the $[EMIm^+][FSI^-]$ Ionic Liquid Confined in Micro- and Mesoporous Carbons. *J. Mater. Chem. A* **2022**, *10* (14), 7928−7940.
(63) Makino, T.; Kanakubo, M.; Masuda, Y.; Umecky, T.; Suzuki, A. CO_2 Absorption Properties, Densities, Viscosities, and Electrical Conductivities of Ethylimidazolium and 1-Ethyl-3-methylimidazolium Ionic Liquids. *Fluid Phase Equilib.* **2014**, *362*, 300−306.
(64) Schilderman, A. M.; Raeissi, S.; Peters, C. J. Solubility of Carbon Dioxide in the Ionic Liquid 1-Ethyl-3-methylimidazolium Bis-(Trifluoromethylsulfonyl)imide. *Fluid Phase Equilib.* **2007**, *260* (1), 19−22.
(65) Huang, K.; Peng, H.-L. Solubilities of Carbon Dioxide in 1-Ethyl-3-methylimidazolium Thiocyanate, 1-Ethyl-3-methylimidazolium Dicyanamide, and 1-Ethyl-3-methylimidazolium Tricyanomethanide at (298.2 to 373.2) K and (0 to 300.0) KPa. *J. Chem. Eng. Data* **2017**, *62* (12), 4108−4116.
(66) Chen, Y.; Mutelet, F.; Jaubert, J.-N. Solubility of Carbon Dioxide, Nitrous Oxide and Methane in Ionic Liquids at Pressures Close to Atmospheric. *Fluid Phase Equilib.* **2014**, *372*, 26−33.
(67) Finotello, A.; Bara, J. E.; Camper, D.; Noble, R. D. Room-Temperature Ionic Liquids: Temperature Dependence of Gas Solubility Selectivity. *Ind. Eng. Chem. Res.* **2008**, *47* (10), 3453−3459.
(68) Chen, D.; Ying, W.; Guo, Y.; Ying, Y.; Peng, X. Enhanced Gas Separation through Nanoconfined Ionic Liquid in Laminated MoS_2 Membrane. *ACS Appl. Mater. Interfaces* **2017**, *9* (50), 44251−44257.

https://doi.org/10.1021/acsami.4c21064
ACS Appl. Mater. Interfaces 2025, 17, 11348−11361